Subsurface Zonal and Meridional Flow Derived from GONG and SDO/HMI: A Comparison of Systematics

R. Komm[1] · I. González Hernández[1] · R. Howe[2] · F. Hill[1]

Abstract We study the subsurface flows in the near-surface layers of the solar convection zone from the surface to a depth of 16 Mm derived from *Global Oscillation Network Group* (GONG) and *Helioseismic and Magnetic Imager* (HMI) Dopplergrams using a ring-diagram analysis. We characterize the systematic east–west and north–south variations present in the zonal and meridional flows and compare flows derived from GONG and HMI data before and after the correction. The average east–west variation with depth of one flow component resembles the average north–south variation with depth of the other component. The east–west variation of the zonal flow together with the north–south variation of the meridional flow can be modeled as a systematic radial velocity. This indicates a solar center-to-limb variation as the underlying cause. The north–south variation of the zonal flow and the east–west variation of the meridional flow require two separate functions. The east–west variation of the meridional flow consists mainly of an annual variation with the B_0 angle, while the north–south trend of the zonal flow consists of a constant non-zero component in addition to an annual variation. This indicates a geometric projection artifact. After compensating for these systematic effects, the meridional and zonal flows derived from HMI data agree well with those derived from GONG data. An offset remains between the zonal flow derived from GONG and HMI data. The equatorward meridional flows at high latitude that appear episodically depending on the B_0 angle are absent from the corrected flows.

Keywords Helioseismology, observations · Velocity fields, interior

---

I. González Hernández is deceased.

✉ R. Komm
komm@nso.edu

[1]   National Solar Observatory, Tucson, AZ 85719, USA

[2]   University of Birmingham, Edgbaston, Birmingham B15 2TT, UK

1. Introduction

Subsurface flows have been derived with time-distance or ring-diagram analysis in the near-surface layers of the Sun using different instruments, such as the *Michelson Doppler Imager* (MDI) instrument (Scherrer *et al.*, 1995) onboard the *Solar and Heliospheric Observatory* (SOHO) and the ground-based *Global Oscillation Network Group* (GONG) instruments (Harvey *et al.*, 1996). For reviews of techniques and instruments used in local helioseismology, we refer to Gizon, Birch, and Spruit (2010) and Gizon and Birch (2005). In previous studies (Komm, Howe, and Hill, 2009, 2011; Komm *et al.*, 2013), we have reported that these flows show systematic variations with disk position in daily flow maps. These systematics have to be corrected in studies of the evolution of subsurface flows associated with active regions; otherwise changes in disk position can be mistaken for temporal evolution. The variations in the zonal flow have been reported in time-distance measurements as well (Zhao *et al.*, 2012).

Zhao *et al.* (2012) have measured the meridional flow with a time-distance analysis using data from the *Helioseismic and Magnetic Imager* (HMI) instrument (Scherrer *et al.*, 2012; Schou *et al.*, 2012) onboard the *Solar Dynamics Observatory* (SDO) spacecraft and found that the flow amplitudes were different between Dopplergrams and intensity measurements. They reported that the zonal flow along the equator showed a variation from east to west and assumed that this systematic variation could be used to correct the corresponding meridional flow along the central meridian. The meridional flows derived from Dopplergrams and intensity data were much closer after this correction. Baldner and Schou (2012) have suggested that a radial velocity component might be introduced as a bias due to the varying height of the spectral-line formation from disk center to the solar limb in the solar atmosphere. The projection of such a radial component would lead to an east–west trend in the zonal flow and to a north–south trend in the meridional flow. Greer, Hindman, and Toomre (2013) have mapped the systematic variations as functions of disk position for HMI data covering multiple Carrington rotations.

Another systematic effect is the annual variation with the solar inclination toward Earth, or B_0 angle, which can lead to a loss in spatial resolution and increase the flow errors. For a large positive B_0 angle value, a location at a given latitude in the northern hemisphere is located closer to disk center than a location at the same latitude in the southern hemisphere, while it is the opposite for large negative B_0 angle values. A large positive or negative B_0 angle value will thus increase the geometric foreshortening and lower the effective spatial resolution in either the southern or the northern hemisphere. The variation of the B_0-angle leads to strong annual variations in the meridional flow at moderate to high latitudes (Zaatri *et al.*, 2006; González Hernández *et al.*, 2008; Komm *et al.*, 2013).

In this study, we empirically derive a functional form of these systematic effects and discuss the benefits of correcting the horizontal flows. We follow the insight by Baldner and Schou (2012), who described the systematics as radial velocity fields , and derive these functions for GONG and HMI Dopplergrams. We focus on the systematic variations with disk position of subsurface velocities as a function of depth. From our previous studies (Komm, Howe, and Hill, 2011), we know that there are additional systematic variations, such as an east–west variation in the meridional flow and a north–south variation in the zonal flow. We describe these variations also as functions of the distance from disk center and determine their dependence on the B_0 angle. We then compare the average zonal and meridional flows derived from GONG and HMI data with and without correction to show their effect.

2. Data and Ring-Diagram Analysis

We analyzed full-disk Dopplergrams obtained with the GONG network and the HMI instrument. The GONG data cover 161 Carrington rotations (26 July 2001 – 30 July 2013; http://gong.nso.edu/data), while the HMI data were obtained during 52 Carrington rotations (2 May 2010 – 6 April 2014). We determine the horizontal components of solar subsurface flows with a ring-diagram analysis using the dense-pack technique (Haber *et al.*, 2002) adapted to GONG data (Corbard *et al.*, 2003) and to HMI data processed by the HMI ring-diagram pipeline (Bogart *et al.*, 2011a, 2011b). Full documentation on the HMI pipeline analysis modules and associated data products can be found on the web pages of the HMI Ring Diagrams Team (http://hmi.stanford.edu/teams/rings/). HMI pipeline results are available through the Joint Science Operations Center or JSOC (http://jsoc.stanford.edu).

The GONG full-disk Doppler images were divided into 189 overlapping regions with centers spaced by 7.5° ranging over ±52.5° in latitude and central meridian distance (CMD). The data were analyzed in "days" of 1664 min, and each region was apodized with a circular function reducing the effective diameter to 15° before calculating three-dimensional power spectra. Each of these regions was tracked throughout the sequence of images using the surface rate (Snodgrass, 1984) appropriate for the center of each region as tracking rate. For each dense-pack day, we derived maps of horizontal velocities at 189 locations in latitude and CMD for 16 depths from 0.6 to 16 Mm.

The HMI full-disk Doppler images were divided into 284 or 281 overlapping tiles also with an effective diameter of 15° after apodization. The number and distribution of tiles varies with the solar inclination toward Earth or the B_0 angle (Bogart *et al.*, 2011b), and the centers of the tiles range up to ±75° in latitude and CMD. The tile centers are spaced by 7.5° in latitude, while in CMD the centers are spaced by 7.5° up to a latitude of 30°, but sparser at higher latitudes. To create a uniformly spaced grid at high latitudes, we interpolated the inferred flows linearly in CMD on a grid with centers spaced by 7.5° in CMD. The Carrington rotation rate was used as the tracking rate for HMI data and not a differential rotation rate as in the case of GONG data. Since a constant rotation rate was used for each tile, the rotation rate varies over each tile. This is small at low latitudes but can be on the order of 10 % at latitudes near 60° and higher. We assume that this variation either averages out or adds only higher-order effects at most.

To remove the average differential rotation in the HMI data, we subtracted the difference between the two tracking rates. As with GONG data, we derived daily maps of horizontal velocities for each tile at each depth. Throughout this study, we refer to the centers of the ring-diagram tiles when mentioning latitude or CMD values.

For this study, we created disk-averaged flow maps for each depth of each Carrington rotation by averaging 24 daily flow maps as a function of disk position in CMD and latitude. This kind of map has been used by Haber *et al.* (2002) to study the systematic variations shown in flow maps derived from a ring-diagram analysis of MDI Dynamics Program Dopplergrams. Figures 1 and 2 show examples of disk-averaged flow maps derived from GONG and HMI Dopplergrams averaged over several Carrington rotations grouped by the B_0 angle. In addition to disk-averaged flow maps, we created synoptic flow maps by combining daily flow maps from GONG and HMI. For each Carrington longitude in a given synoptic map, we averaged the corresponding daily values using a weighting factor of cosine CMD to the fourth power, as in the maps of magnetic activity created at NSO/Kitt Peak (Harvey *et al.*, 1980).
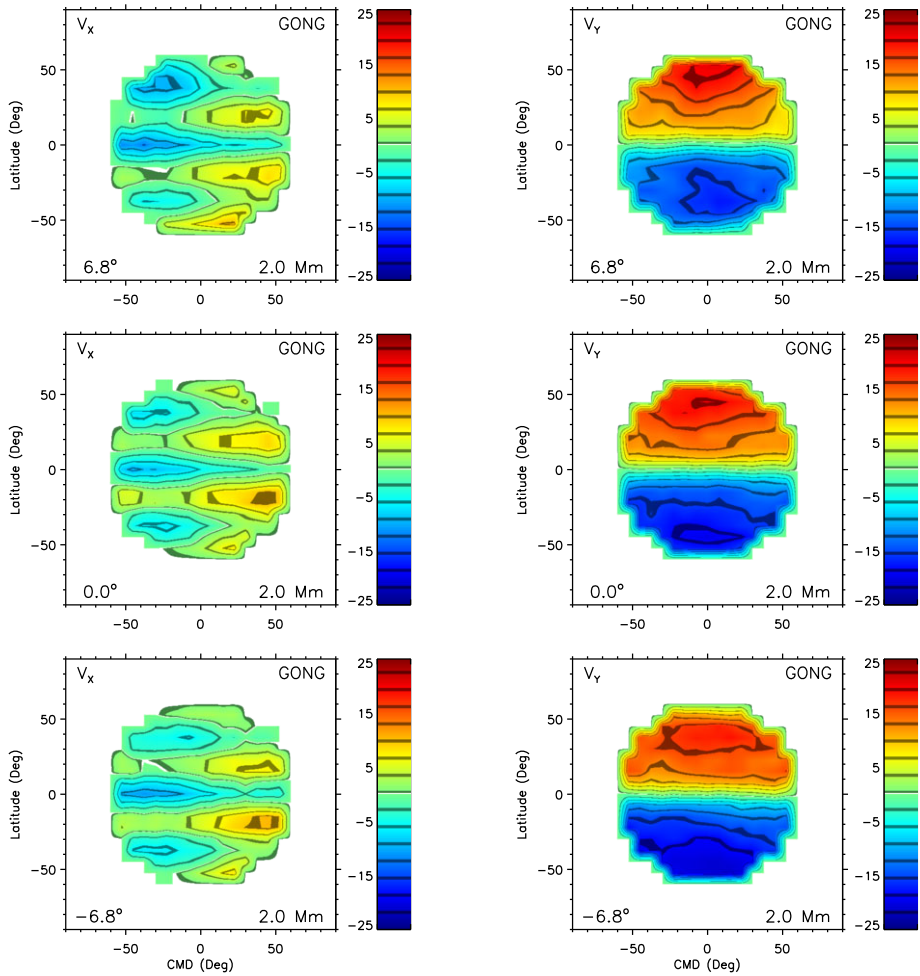
Figure 1 The disk-averaged zonal (left) and meridional (right) flow (in m s^{-1}) from GONG data averaged as a function of CMD and latitude over 30 Carrington rotations with large positive B_0 angles, 29 rotations with zero, and 30 rotations with large negative B_0 angles (top: $B_0 > 6°$; middle: $|B_0| \leq 2°$; bottom: $B_0 < -6°$) at a depth of 2.0 Mm. The average B_0 angles are 6.8°, 0.0°, and −6.8° from top to bottom. The average zonal flow as a function of latitude has been subtracted (left); positive values of the meridional flow indicate flows to the north (right), negative values indicate flows to the south.

3. Results

3.1. Systematic Variation with Disk Position

In this section, we focus on the systematic variation with disk position of the zonal and meridional flow derived from GONG and HMI Dopplergrams using ring-diagram analysis. Figures 1 and 2 show the observed disk-averaged flow maps at a depth of 2.0 Mm averaged over several Carrington rotations for three ranges of the B_0 angle. The average zonal flow at a depth of 4.4 Mm was subtracted to compensate for the average differential rotation; this rate works well for the whole depth range used. The average zonal flow
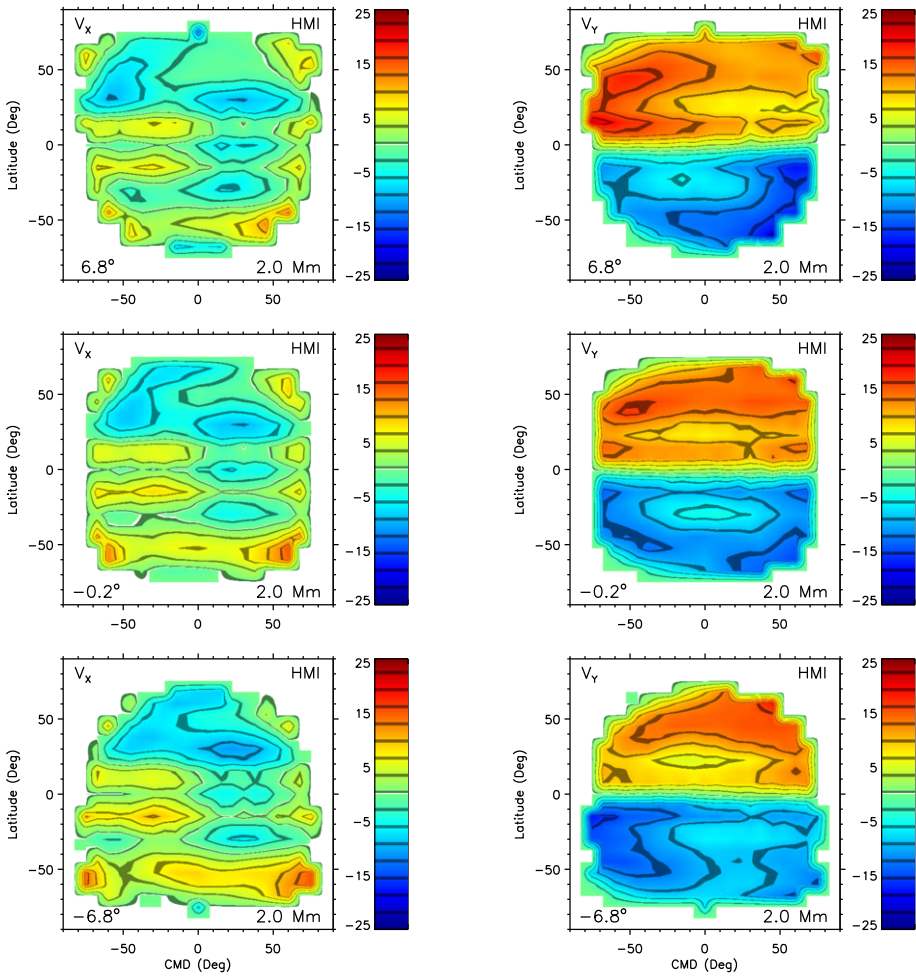
Figure 2 The disk-averaged zonal (left) and meridional (right) flow $(m\,s^{-1})$ from HMI data averaged as a function of CMD and latitude over 10 Carrington rotations with large positive B_0 angles, 9 rotations with zero, and 10 rotations with large negative B_0 angles (top: $B_0 > 6°$; middle: $|B_0| \leq 2°$; bottom: $B_0 < -6°$) at a depth of 2.0 Mm. The average B_0 angles are $6.8°$, $-0.2°$, and $-6.8°$ from top to bottom. The average zonal flow as a function of latitude has been subtracted (left); positive values of the meridional flow indicate flows to the north (right), negative values indicate flows to the south. (Compare with Figure 1.)

(left column of Figures 1 and 2) shows a strong east–west variation. We have chosen this depth to illustrate that the direction of this trend can be different between different instruments. The zonal flow derived from GONG data increases from east to west, while that derived from HMI data decreases from east to west. The corresponding meridional flow from HMI data (Figure 2; right column) also shows a strong east–west trend, which changes sign between large positive and negative B_0-angle values. The meridional flow from GONG data (Figure 1; right column) shows mainly a CMD variation with a minimum or maximum at the central meridian depending on hemisphere and very large or small values at extreme limb positions at a given latitude, with some variation due to the B_0 angle. The effect of the B_0 angle on the zonal flow is a small variation in the north–south trend. The
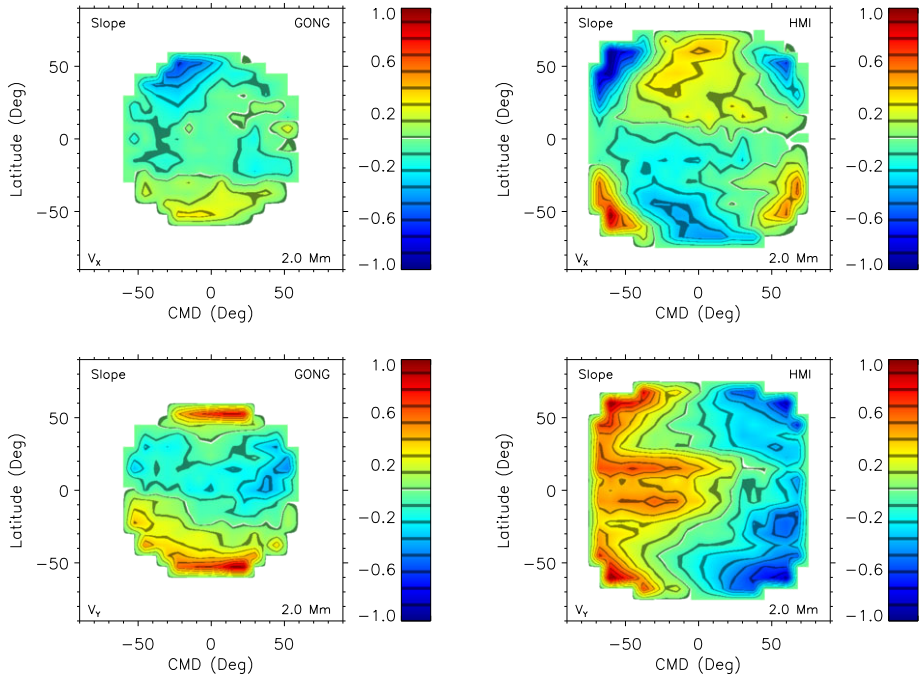
Figure 3 The slope of a linear regression (in $m\,s^{-1}\,degree^{-1}$) with the B_0 angle for the zonal (top) and meridional flow (bottom) from GONG (left) and HMI data (right) at a depth of 2.0 Mm. The values are calculated from the full-disk maps of 161 Carrington rotations (GONG) and 52 Carrington rotations (HMI).

zonal flow from GONG data is lower in the northern hemisphere than in the southern one for large positive B_0 angle values and higher for large negative B_0 angles. The zonal flow from HMI data shows the opposite behavior. The overall north–south trend with higher zonal-flow values in the southern than in the northern hemisphere was removed by removing the average flow at 4.4 Mm. As expected from previous studies (Zaatri *et al.*, 2006; González Hernández *et al.*, 2008), the meridional flow varies with the B_0 angle, showing large amplitudes in the northern hemisphere for large positive B_0 angles and large amplitudes in the southern hemisphere for large negative B_0 angles.

To determine the variation with the B_0 angle, we performed a linear regression with B_0 for both flow components at each disk position. Figure 3 shows the resulting slopes at 2.0 Mm as a function of disk position derived from GONG and HMI data. The magnitude of the B_0 variation is similar between zonal and meridional flow. The slope is nearly symmetric across the equator for the meridional flow and antisymmetric for the zonal flow. For the zonal flow, a positive slope in the northern hemisphere implies the same as a negative slope in the southern one; the flow amplitude is greatest when the solar inclination leads to the smallest geometric foreshortening in a given hemisphere (maximum B_0 in the northern and minimum B_0 in the southern hemisphere). For the meridional flow, a positive slope in either hemisphere implies the same because the average flow changes sign at the equator. The largest variations with the B_0 angle occur mainly at high latitudes, and the slope is small near the equator, as expected. However, the slopes also show an east–west variation, which is especially noticeable in the HMI meridional flow data. The east–west variation seems to be smaller for the meridional flow derived from GONG data.
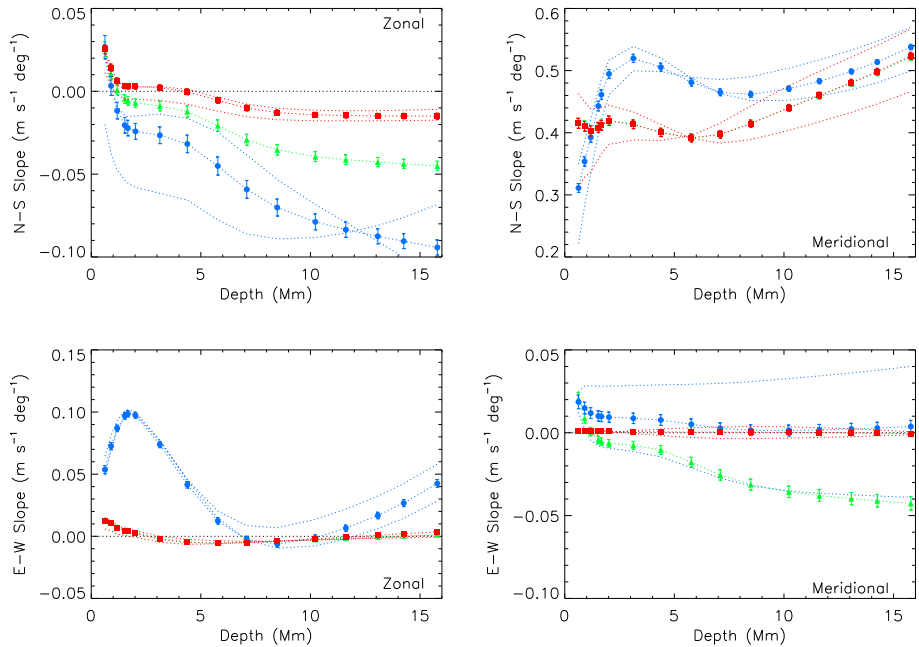
Figure 4 The average slope (in $\mathrm{m\,s^{-1}\,degree^{-1}}$) of a linear regression in the north–south (top) and the east–west direction (bottom) of the zonal (left) and meridional flow (right) from GONG data as a function of depth averaged over 161 full-disk flow maps. The symbols represent the original values (blue circles), the values corrected with a radial and a rotational term (green triangles; Equations (3) and (4)), and the ones corrected with a radial and two additional terms (red squares; Equations (5) and (6)). The red and green curves are nearly identical in the top right and bottom left panels. The averages over maps with large positive or large negative B_0 angles ($B_0 > 6°$ or $B_0 < -6°$) are indicated as dotted lines.

We measured the east–west and north–south variations of the subsurface flows by performing a linear regression in each direction in CMD or latitude of the meridional and zonal flow. We included the disk positions between $\pm 45°$ CMD and latitude for GONG and $\pm 60°$ for HMI data and calculated the regression slopes for each disk-averaged flow map. Figures 4 and 5 show the resulting slopes for GONG and HMI data (blue circles) as functions of depth averaged over all Carrington rotations. The meridional flow is mainly positive in the northern and negative in the southern hemisphere, which leads to a large positive slope in the north–south variation (top right of Figures 4 and 5). However, it is interesting that its variation with depth resembles the east–west variation of the zonal flow (bottom left) in shape and magnitude. This similarity indicates that the underlying cause might be a radial velocity field, as suggested by Baldner and Schou (2012).

Similarly, the average variation with depth of the north–south trend of the zonal flow (top-left) resembles that of the east–west trend of the meridional flow (bottom-right). These two trends show somewhat larger variations with the B_0 angle than the other two variations. This similarity might imply that the underlying cause is a rotation around disk center that might be introduced, for example, by a misalignment of the solar rotation axis in the Dopplergrams. A temporal variation in the P-angle leads to an apparent rotation around disk center, the so-called washing-machine effect (reported by Corbard *et al.*, 2003). Such a systematic velocity would be orthogonal to a radial velocity component, and its projection onto the zonal and meridional velocities would lead to the corresponding north–south and east–west variation.
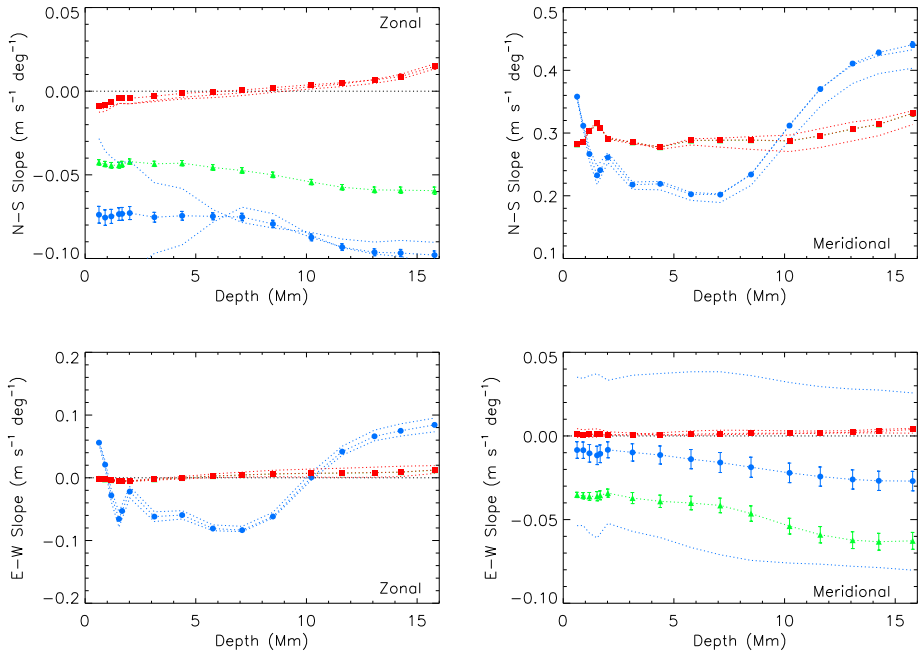
Figure 5 The average slope (in $m\,s^{-1}\,degree^{-1}$) of a linear regression in the north–south (top) and the east–west direction (bottom) of the zonal (left) and meridional flow (right) from HMI data as a function of depth averaged over 52 full-disk flow maps. The symbols represent the original values (blue circles), the values corrected with a radial and a rotational term (green triangles; Equations (3) and (4)), and the values corrected with a radial and two additional terms (red squares; Equations (5) and (6)). The red and green curves are identical in the top right and bottom left panels. The averages over maps with large positive or large negative B_0 angles ($B_0 > 6°$ or $B_0 < -6°$) are indicated as dotted lines. (Compare with Figure 4.)

However, while the shape is similar between the two variations with depth, the magnitudes are different. The change from the surface to a depth of 16 Mm is much greater in the north–south trend of the zonal flow than in the east–west variation of the meridional flow. The different magnitude implies that a potential P-angle error does not explain these variations (at least not completely).

We determined these systematic variations assuming that the underlying functions vary only with distance from disk center. We started with two terms where the first describes a systematic radial velocity component, and the second describes a systematic rotation around the disk center assuming that the perturbations are linear and additive. Each term is described by a set of polynomials, which are required to be orthogonal on the disk. The distance from disk center (r) is defined as

$$r^2 = (\sin\phi\cos\theta)^2 + (\sin\theta\cos B_0 - \cos\theta\sin B_0\cos\phi)^2, \tag{1}$$

where the first term represents the east–west and the second represents the north–south distance from disk center (T. Duvall, private communication) with latitude (θ), CMD (ϕ), and B_0 angle and disk center at $r = 0$ and the solar limb at $r = 1$. For simplicity, we rewrite Equation (1) as follows:
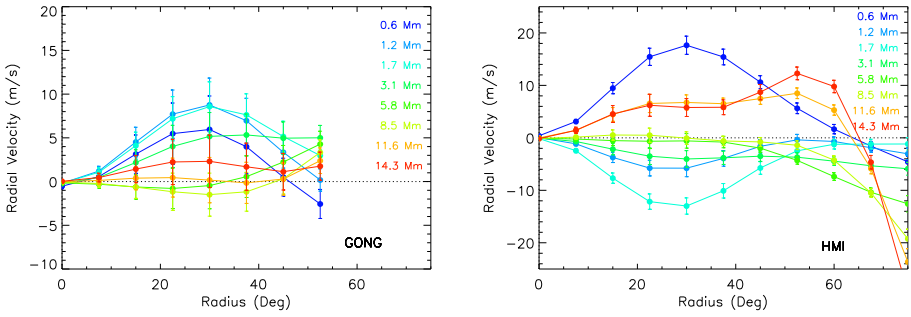
$$r^2 = x^2 + y^2, \tag{2}$$

Figure 6 The average radial velocity artifact (in m s^{-1}) derived from GONG (left) and HMI data (right) at eight depths (blue: 0.6 Mm; red: 15.8 Mm). The error bars indicate the standard deviation of the distributions. The curves are symmetric across $r = 0$.

where x and y represent the first and second term of Equation (1), respectively. The resulting radial velocity component has to be zero at disk center. To also ensure a continuous (zero) derivative, we have chosen the radial polynomials $[R_n^m(r)]$ of Zernike polynomials with $m = 2$ and $n = 2, 4, 6, 8$ where $R_2^2 = r^2$ is the first polynomial. We can then represent the zonal and meridional flow (v_x and v_y) as

$$v_x^{\text{obs}}(\theta, \phi) = v_x + x \sum_{i=1}^{4} a_i R_{2i}^2(r) - y \sum_{i=1}^{2} \tilde{b}_i R_{2i}^2(r), \tag{3}$$

$$v_y^{\text{obs}}(\theta, \phi) = v_y + y \sum_{i=1}^{4} a_i R_{2i}^2(r) + x \sum_{i=1}^{2} \tilde{b}_i R_{2i}^2(r), \tag{4}$$

where v_x^{obs} and v_y^{obs} are the measured velocities of the disk-averaged maps of each Carrington rotation at every depth. We fit the observed velocities and determine the coefficients a_i and $\tilde{b}_i$, which represent the systematic radial and rotational velocity component for each depth and Carrington rotation. We varied the maximum order of polynomials using the slopes shown in Figures 4 and 5 as guidance and found that we can fit the systematic radial velocity in HMI and GONG data with four and three radial polynomials, respectively. For the systematic rotational velocity, we used two radial polynomials to fit the disk-averaged flow maps.

For the meridional flow, we subtracted the mean at every latitude from the flow and the fitting function and fit the residual flow with the residual function because otherwise the fitting procedure would treat most of the meridional flow as a north–south trend to be removed. In principle, we would have liked to simultaneously fit a function of latitude to the meridional flow. However, the flow amplitude varies with the presence of magnetic activity at a given latitude, and the amount of magnetic activity is not symmetric across the equator. This would lead to a much more complex fitting procedure because we would have to adequately fit the influence of magnetic activity as well in order to avoid introducing a "magnetic" north–south trend.

Figure 6 shows the resulting systematic radial velocity components as functions of distance from disk center. In Figures 6 and 7, the distance from disk center is given in degree, ranging from 0° to 90°, in order to coincide with the ring-diagram grid. The radial components derived from GONG data are positive at most depths and distances from disk center, while those from HMI data are negative at intermediate depths. The maximum amplitude of

the radial velocity component occurs near 22.5° or 30° in GONG and HMI measurements at most depths. The maximum amplitude derived from HMI data is generally larger than that from GONG data. At depths greater than about 10 Mm, there is a second maximum near 52.5° in HMI data. The radial velocity components from GONG and HMI do not vary much with the B_0 angle.

As a test, we did not enforce a continuous derivative at disk center. In this case, a series of orthogonal radial polynomials with R_n^1, which includes a linear term ($R_1^1 = r$), can be used. The maximum of the radial velocity artifact is then at 22.5° and the amplitudes at 7.5° to 22.5° are larger. For radial distances of 30° or greater, the radial velocity component is the same with or without continuous derivative at disk center. This choice makes little difference for the corrected flows since the applied correction is small that close to disk center. The fitting procedure is robust with regard to the choice of polynomials.

The corresponding east–west and north–south trends present in the zonal and meridional velocities after correcting for these systematic velocity components are included in Figures 4 and 5 (green triangles). The east–west trend of the zonal flow is nearly zero after this correction, and the corresponding north–south trend of the meridional flow is non-zero, but nearly constant with depth compared with the uncorrected trend. The radial velocity component is an adequate description of these systematics. The north–south trend of the zonal flow is reduced by about half, but the corresponding east–west trend of the meridional flow has increased by a similar amount. Both trends are about the same size after the correction. The increase of the east–west trend of the meridional flow indicates that the underlying cause of this artifact is not simply a rotational velocity component.

The problem with the east–west trend of the meridional flow is that it changes sign with the B_0 angle. A rotational velocity component might be adequate to describe the systematics for negative B_0 values. However, the sign is reversed for most positive B_0 values, which superficially implies a velocity field where the flows in two opposite quadrants are toward the disk center and the flows in the other two are away from the disk center. To account for this, we have added a third term to Equations (3) and (4) similar to the second term with the opposite sign in the meridional flow part. The second and third term are not orthogonal and have to be fit sequentially; the first and second term are fit together first and then the third term is fit to the residual. This scheme implies that the north–south variation of the zonal velocity is decoupled from the east–west variation of the meridional flow, and we can equally well fit them independently of each other:

$$v_x^{\text{obs}}(\theta, \phi) = v_x + x \sum_{i=1}^{4} a_i R_{2i}^2(r) - y \sum_{i=1}^{2} c_i R_{2i}^2(r),$$ (5)

$$v_y^{\text{obs}}(\theta, \phi) = v_y + y \sum_{i=1}^{4} a_i R_{2i}^2(r) + x \sum_{i=1}^{2} b_i R_{2i}^2(r),$$ (6)

where the a_i coefficients represent the radial velocity component as in Equations (3) and (4), while b_i and c_i are the fitting coefficients representing the east–west variation of the meridional flow and the north–south variation of the zonal flow, respectively. This procedure greatly reduces the north–south trend of the zonal flow and the east–west trend of the meridional flow, as shown in Figures 4 and 5 (red squares). In addition, the variation with the B_0 angle is greatly reduced, as indicated by the dotted lines. The east–west trend of the
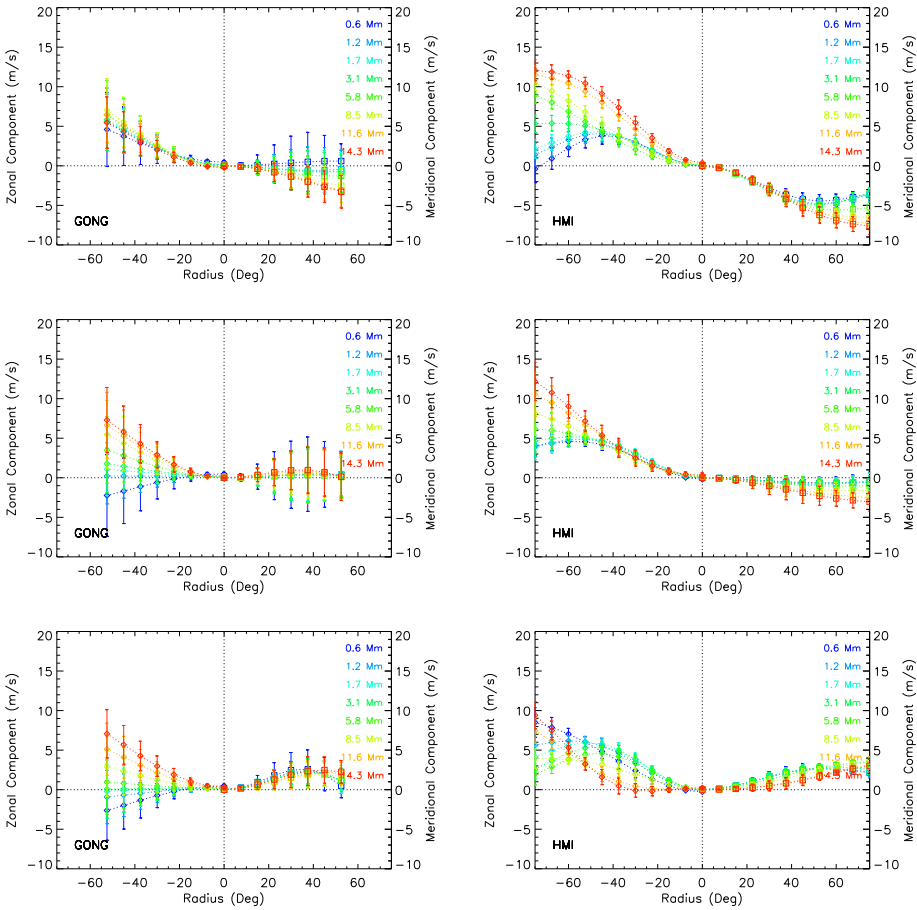
Figure 7 The average zonal-velocity (diamonds) and the average meridional-velocity artifact (squares) in $\mathrm{m\,s^{-1}}$) derived from GONG (left) and HMI data (right) at eight depths (blue: 0.6 Mm; red: 15.8 Mm) for large positive B_0 angles (top; $B_0 > 6°$), zero B_0 angles (middle; $|B_0| \leq -2°$), and large negative B_0 angles (bottom; $B_0 < -6°$). The error bars indicate the standard deviation of the distributions. To show both radial functions in the same figure, we depict the zonal-velocity artifact at "negative" radius values for simplicity. (Compare with Figure 6.)

zonal flow and the north–south trend of the meridional flow remain more or less unchanged by this modification.

Figure 7 shows the resulting systematic velocity components of the zonal and meridional flows as functions of distance from disk center. The systematic velocity functions derived from GONG and HMI are very similar in size and sign. The meridional component changes sign with the B_0 angle. The zonal component is mainly positive, with a generally larger amplitude than the meridional one and changes with the B_0 angle as well. We used only the first term to fit the north–south trend of the zonal flow of GONG data and two radial polynomials to fit the other trends.

We now focus on the temporal variation of the derived systematic functions. Figure 8 shows the first-order fitting parameters as functions of time and depth derived from HMI data. The radial velocity component is more or less constant with time at all depths, with
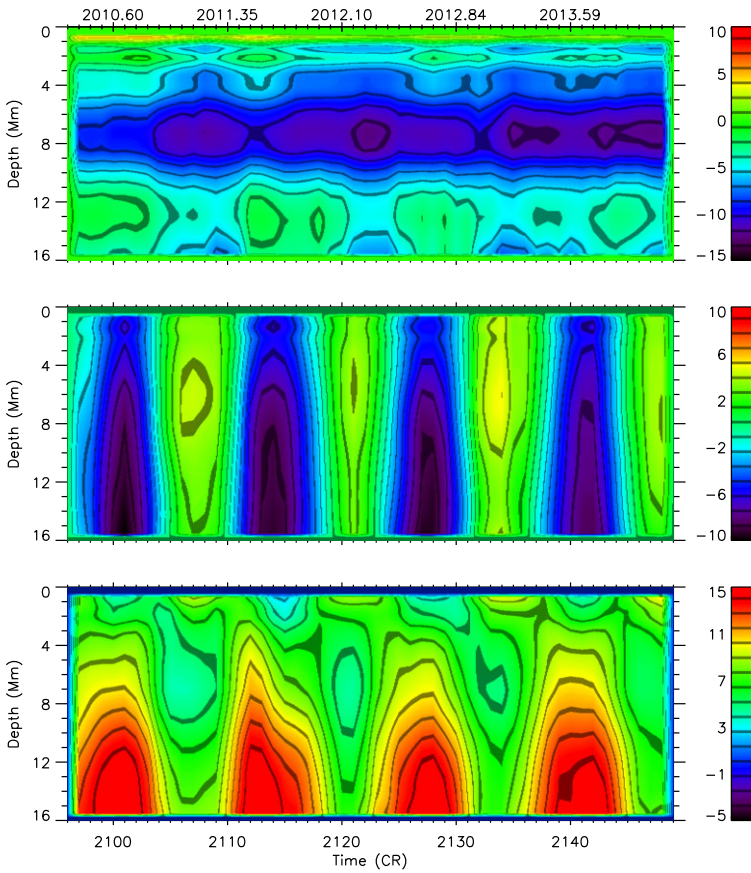
Figure 8 The first-order fitting coefficients (Equations (5) and (6); in $\mathrm{m\,s^{-1}}$) of the radial (top), the meridional (middle), and the zonal component (bottom) derived from HMI data as functions of time and depth. The data have been smoothed via three-CR moving-window averaging.

only a hint of a small decrease with time and an annual variation with a comparatively small amplitude of about 3 $\mathrm{m\,s^{-1}}$ or less between maximum and minimum B_0 value. The meridional and the zonal component clearly vary much more with an annual period that is in phase with the B_0 angle. The meridional component is anticorrelated with the B_0 angle at all depths, while the zonal component is correlated at depths greater than about 4 Mm and anticorrelated at shallower depths. The difference between maximum and minimum B_0 value is about 8 $\mathrm{m\,s^{-1}}$ for the zonal component and about 12 $\mathrm{m\,s^{-1}}$ for the meridional one.

Figure 9 shows the same as Figure 8 after fitting a linear function of B_0 angle and solar radius to remove the annual variation. The apparent solar radius has to be included in the fitting in addition to B_0 to greatly reduce the annual variation. The radial component is essentially unchanged. The meridional component is constant with time and decreases from about -1 $\mathrm{m\,s^{-1}}$ to -3 $\mathrm{m\,s^{-1}}$ with increasing depth. The zonal component is also constant with time and is about 6 $\mathrm{m\,s^{-1}}$ at depths less than about 6 Mm and about 11 $\mathrm{m\,s^{-1}}$ at 16 Mm. The zonal component shows a half-year periodicity at greater depth (bottom panel), which is due to the combined effect of the correction and the increase in noise in the data with
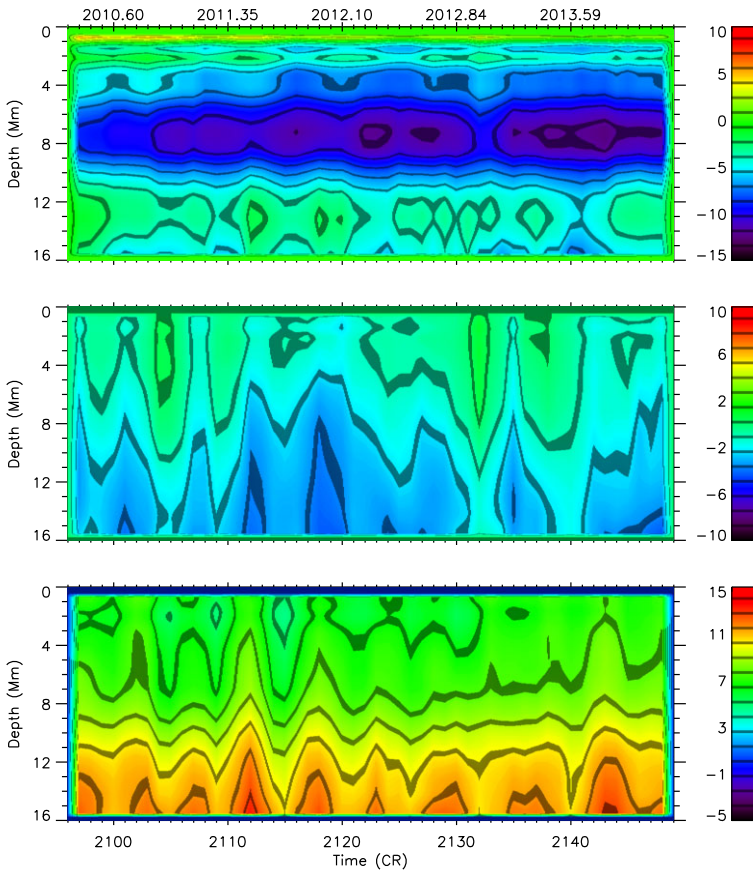
Figure 9 The first-order fitting coefficients (Equations (5) and (6); in m s^{-1}) of the radial (top), the meridional (middle), and the zonal component (bottom) derived from HMI data as functions of time and depth after removing the annual variation with the B_0 angle and the apparent solar radius. The data have been smoothed via three-CR moving-window averaging. (Compare with Figure 8.)

increasing depth. The other fitting parameters show a similar behavior. The parameters of the radial component are rather constant with time and show a weak annual variation with small amplitude, while the parameters of the other two components show no long-term trend, but vary with B_0 and the apparent solar radius.

The temporal variations of the systematic functions derived from GONG data exhibit a similar behavior (not shown). The parameters of the radial component fluctuate with time without apparent long-term trend or annual variation. The parameters of the zonal and meridional component vary with B_0 and show no long-term trend either. The meridional component is anticorrelated with the B_0 angle at all depths, while the zonal component is correlated at these depths. For the meridional component, the difference between maximum and minimum B_0 value is about 7 m s^{-1} on average and the parameter is close to zero with -1 m s^{-1} on average after subtracting the annual variation. For the zonal component, the average value increases with depth from zero near the surface to about 10 m s^{-1} at 16 Mm, while the difference between maximum and minimum B_0 value ranges between 12 m s^{-1} and 6 m s^{-1} over
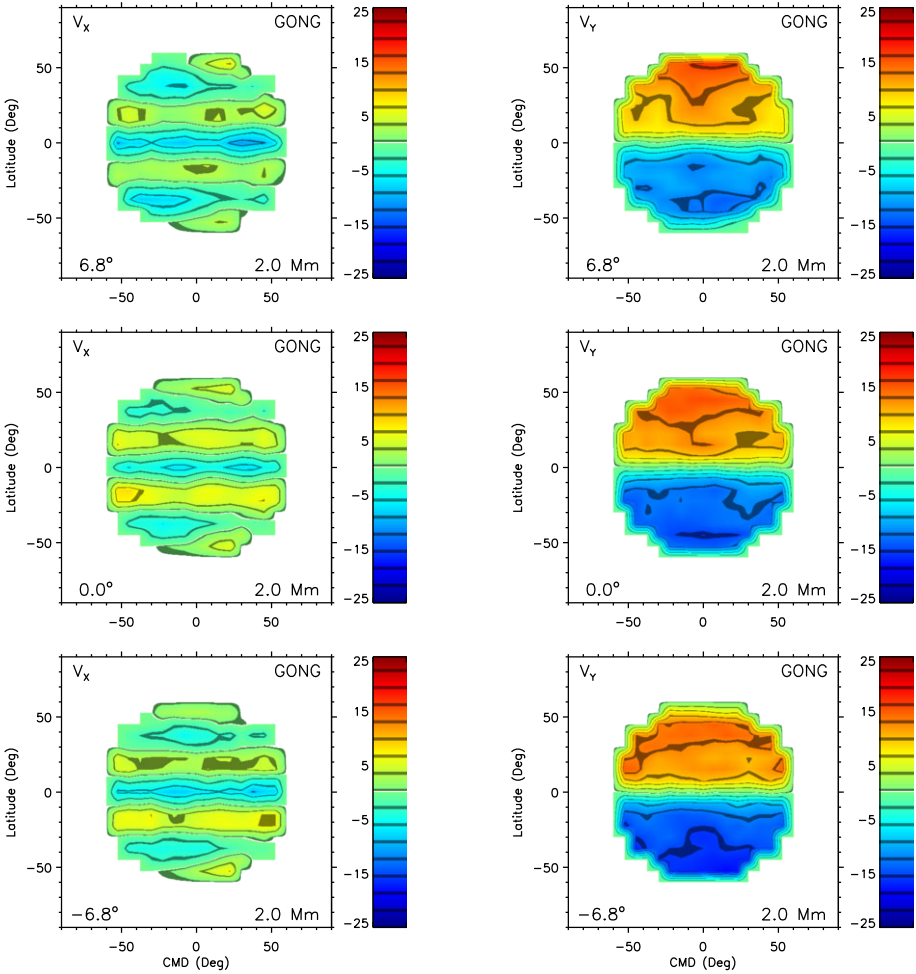
Figure 10 The corrected zonal (left) and meridional flow (right; in m s^{-1}) from GONG data averaged over 30 Carrington rotations with large positive B_0 angles, 29 rotations with zero, and 30 rotations with large negative B_0 angles (top: $B_0 > 6°$; middle: $|B_0| \leq 2°$; bottom: $B_0 < -6°$) at a depth of 2.0 Mm. The average B_0 angles are $6.8°$, $0.0°$, and $-6.8°$ from top to bottom. The average zonal flow as a function of latitude has been subtracted (left); positive values of the meridional flow indicate flows to the north (right), negative values indicate flows to the south. (Compare with Figure 1.)

the same depth range. The meridional component of both GONG and HMI data consists mainly of an annual variation, while the zonal component consists of a non-zero contribution in addition to an annual variation.

Figures 10 and 11 show disk-averaged maps of the corrected zonal and meridional flow. The corrected flows change little with CMD at a given latitude compared to the measured ones shown in Figures 1 and 2. This is especially noticeable in the HMI flow data and in the zonal flow derived from GONG Dopplergrams. For the meridional flow derived from GONG data, the change is not very noticeable at this depth; the main change is a reduction in amplitude. The east–west variation of the corrected flows is the same for all B_0 angle values; the applied correction removes this dependency.
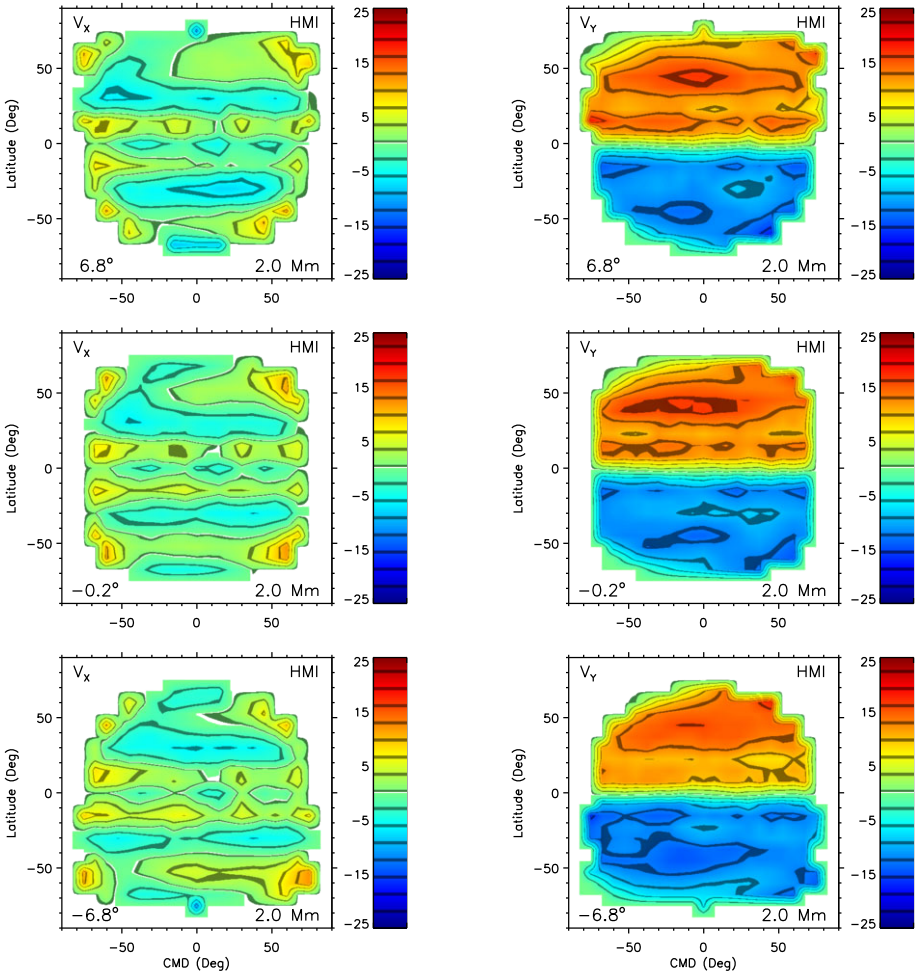
Figure 11 The corrected zonal (left) and meridional flow (right; m s^{-1}) from HMI data averaged over 10 Carrington rotations with large positive B_0 angles, 9 rotations with zero, and 10 rotations with large negative B_0 angles (top: $B_0 > 6°$; middle: $|B_0| \leq 2°$; bottom: $B_0 < -6°$) at a depth of 2.0 Mm. The average B_0 angles are 6.8°, −0.2°, and −6.8° from top to bottom. The average zonal flow as a function of latitude has been subtracted (left); positive values of the meridional flow indicate flows to the north (right), negative values indicate flows to the south. (Compare with Figure 2.)

We performed a linear regression with B_0 angle for the corrected disk-averaged flow maps similar to that shown in Figure 3. The distribution with disk position of the resulting slopes is more uniform with CMD than that from the uncorrected data. In particular the large east–west variation seen in HMI meridional flows (Figure 3, bottom-right) is absent from the corrected values. For the zonal flows, the amplitudes of the slopes are reduced to 0.82 and 0.81 of the values of the uncorrected HMI and GONG data when averaged over all depths. For the meridional flows, the amplitudes of the slopes are reduced to 0.47 and 0.81 of the original slopes derived from HMI and GONG data, respectively. The applied correction thus reduces the variation with the B_0 angle as well.
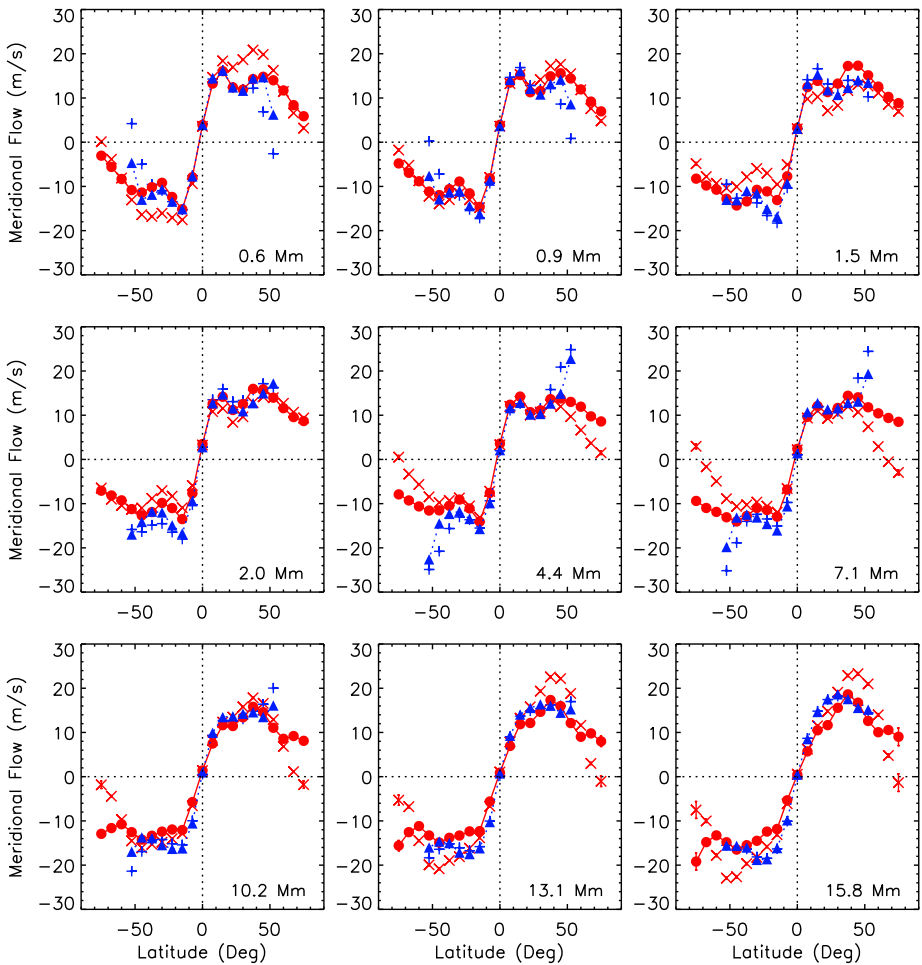
Figure 12 The meridional flow averaged over CR 2097–2138 of HMI data for 9 depths from near-surface (top-left) to deeper layers (bottom-right) corrected for the east–west and north–south systematics and the variation with the B_0 angle (red circles) and without correction (red ×) and the corresponding values from GONG data (blue triangles: corrected; blue crosses: original). Positive values indicate flows to the north, negative values indicate flows to the south. The average B_0 angle is $0.1°$ (the epoch covered is not an integral number of years).

3.2. Comparison of Zonal and Meridional Flow

In this section, we compare the zonal and meridional flows derived from GONG and HMI Dopplergrams covering 42 Carrington rotations (CR) from CR 2097 to 2138. Figure 12 shows the average meridional flow as a function of latitude before and after the correction described in the previous section, while Figure 13 shows the corresponding average zonal flows. The average values of the corrected flows have also been corrected at each latitude for the average variation with the B_0 angle. We performed a linear regression between the B_0 angle and the zonal and meridional flow at each depth and latitude, as in Komm *et al.* (2013). For each latitude, we combined the flow values from both hemispheres by reversing
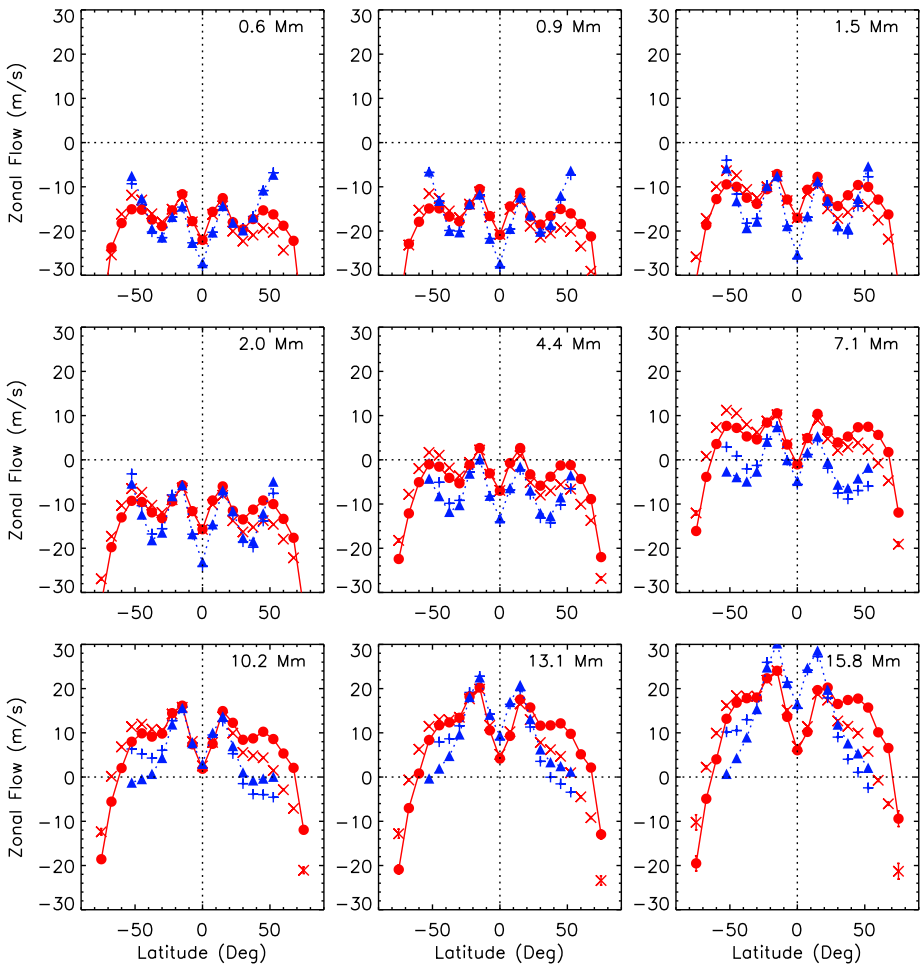
Figure 13 The zonal flow averaged over CR 2097–2138 of HMI data for 9 depths from near-surface (top-left) to deeper layers (bottom-right) corrected for the east–west and north–south systematics and the variation with the B_0 angle (red circles) and without correction (red ×) and the corresponding values from GONG data (blue triangles: corrected; blue crosses: original). An offset of 25 m s^{-1} has been subtracted from each data set. The average B_0 angle is 0.1° (the epoch covered is not an integral number of years).

the sign of B_0 in the southern hemisphere, which is justified given the symmetry across the equator of the B_0 angle slopes shown in Figure 3. We then assumed that the flow values at the maximum B_0 angle of 7.25° are as good as they can be estimated from the observed range of B_0 values, since they represent observations with the highest spatial resolution available (Komm *et al.*, 2013).

For the meridional flows derived from HMI Dopplergrams, the correction reduces the flow amplitudes at low latitudes near the surface and at deeper layers and increases the amplitudes at high latitudes at intermediate and deeper layers (Figure 12). For GONG data, the amplitudes of the meridional flow remain more or less the same at low latitudes, while at high latitudes the correction increases the amplitudes at shallow depths, decreases them at intermediate depths, and does not affect them at greater depths. As a
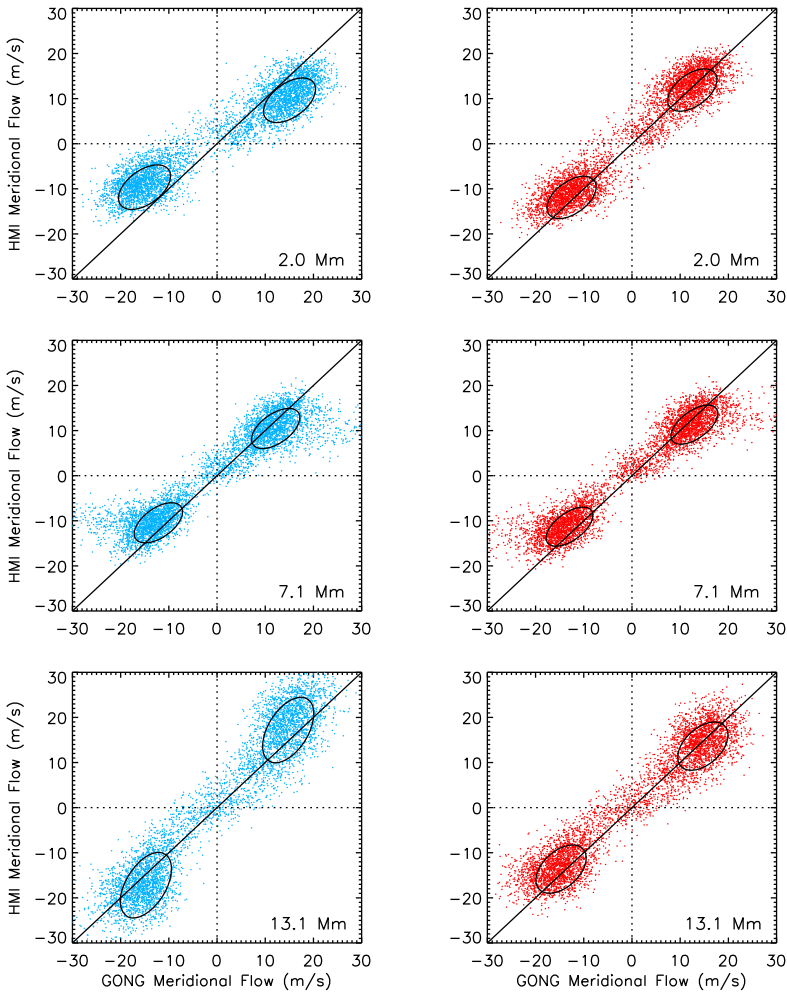
Figure 14 A scatter plot comparing the disk-averaged meridional flow (in m s^{-1}) from GONG data (*x*-axis) with the flow from HMI data (*y*-axis) for the measured (left) and corrected values (right) at three depths (top: 0.6 Mm; middle: 7.1 Mm; bottom: 15.8 Mm) within ±45° latitude and ±30° CMD for 42 Carrington rotations from CR 2097 to 2138. The contours indicate the half maximum of a two-dimensional Gaussian fit to the distributions. For the Gaussian fit, the data of the southern hemisphere have been folded onto the northern one. The contours in both hemispheres are mirror images of each other.

consequence, the corrected meridional flow derived from HMI Dopplergrams is similar in size to that derived from GONG data at high latitudes and nearly identical at low latitudes. In addition, the equatorward flows at high latitude (counter-cells) present in GONG data near the surface and in HMI data at deeper layers are absent from the corrected flows.

Figure 13 shows the same for the average zonal flow. The correction reduces the amplitude of the zonal flow in the southern hemisphere and increases it in the northern one. The average corrected zonal flows from GONG and HMI show similar amplitudes at shallow layers with small values at the equator and local maxima near 15° latitude. The differences
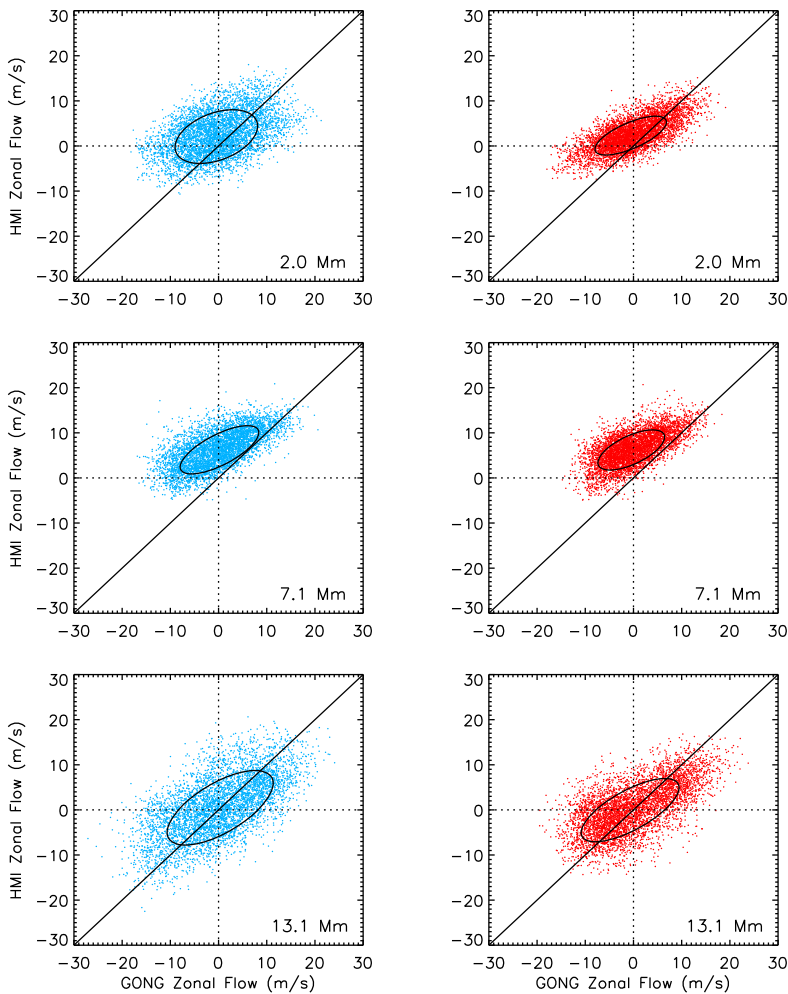
Figure 15 A scatter plot comparing the disk-averaged zonal flow (in m s^{-1}) from GONG data (x-axis) with the flow from HMI data (y-axis) for the measured (left) and corrected values (right) at three depths (top: 0.6 Mm; middle: 7.1 Mm; bottom: 15.8 Mm) within $\pm 45°$ latitude and $\pm 30°$ CMD for 42 Carrington rotations from CR 2097 to 2138. The mean derived from GONG data has been subtracted from each value. The contours indicate the half-maximum of a two-dimensional Gaussian fit to the distributions. (Compare with Figure 14.)

between GONG and HMI zonal-flow values increase with increasing depth, especially at high latitudes.

Next, we compared the disk-averaged flows of the 42 Carrington rotations before and after the correction. Figures 14 and 15 show scatter plots of the meridional and zonal flows derived from GONG and HMI data. For the meridional flow, the data separate into two clouds representing the northern and southern hemisphere (Figure 14). The corrected flows of GONG and HMI are closer in size, with narrower distributions than the uncorrected ones. The widths of the distributions are reduced by about 10 % on average (when fitting a two-dimensional Gaussian distribution). The slope of the distributions is closer to one for the
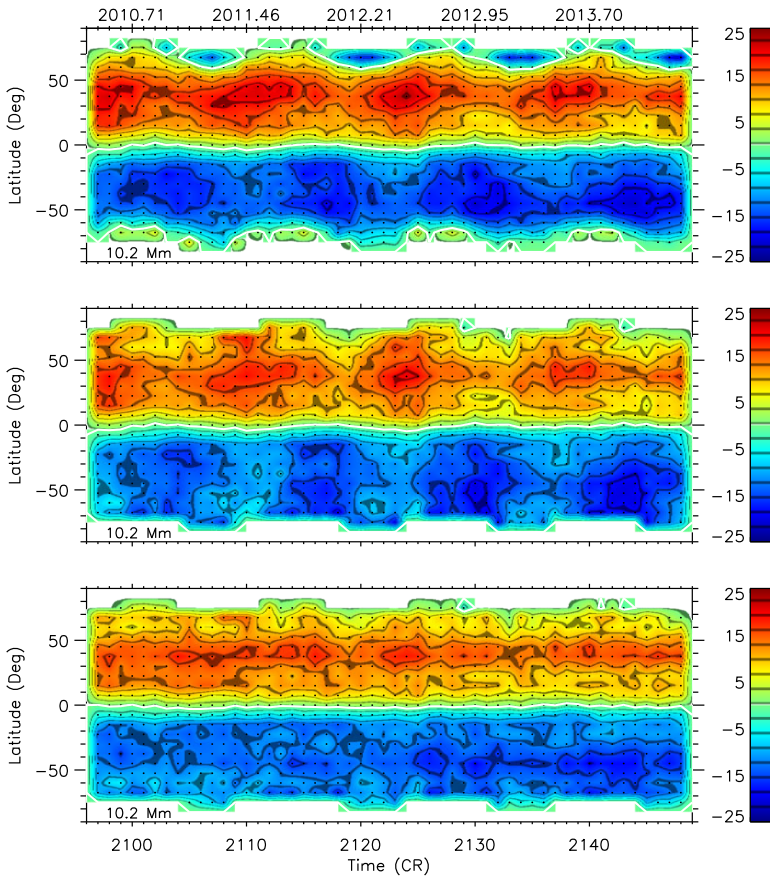
Figure 16 The meridional flow (in m s^{-1}) from HMI data at a depth of 10.2 Mm as a function of time and latitude (top), corrected for the radial and other velocity artifacts (middle), and in addition corrected for the B_0-angle variation and for an annual shift that is 90° out of phase with the B_0 angle (bottom). Positive values indicate flows to the north, negative values indicate flows to the south. The black dots indicate the latitude-time grid. The time coordinate is given in Carrington rotations (bottom x-axis) and calendar years (top x-axis).

corrected data compared to smaller slopes found in the uncorrected flows at shallow layers and larger slopes in deeper layers. For the zonal flow, the correction leads to narrower distributions as well, with a reduction in width of about 20 % on average (Figure 15). This is most pronounced at shallow depths, where the distributions of the corrected flows are more compact than those of the measured flows.

The measured and the corrected zonal flows show an offset between those derived from HMI and GONG data. To see whether this might be due to the different tracking rates, we created scatter plots similar to those shown in Figure 15 with a smaller range in latitude of 30° and an extended range in CMD of 45°. The difference between the tracking rates is small at this latitude range. However, the offsets remain about the same, which indicates that they are not due to the different tracking rates. The slopes of the distributions, on the other hand, are slightly closer to one. The agreement between zonal flows derived from HMI and GONG data is better at lower than at higher latitudes. These comparisons show that across

the solar disk the flows derived from GONG and HMI Dopplergrams are much more alike after the correction.

To illustrate the influence of the correction on the long-term variation of the flows, we show in Figure 16 the meridional flow at a depth of 10.2 Mm as a function of latitude and time derived from HMI data. We have chosen this depth because the measured meridional flow shows counter-cells at the highest latitudes in the northern hemisphere for large negative B_0 angle values and in the southern one at large positive B_0 angles (top). Almost all equatorward flows are removed by the correction of the east–west and north–south variations (middle). The additional B_0-angle correction makes little difference at this depth (bottom).

There is an additional annual variation present that appears as a positive or negative shift at all latitudes for a given epoch (top and middle). This variation has about the same amplitude at all latitudes and depths and is three months (or 90°) out of phase with the B_0 angle, which indicates an error in the P angle as the underlying cause (Beck and Giles, 2005). We can greatly reduce this variation by calculating the average over all latitudes as a function of time, fitting it with a periodic function with the appropriate phase and period, and subtracting the fit from the flow values (bottom). The mean offset is 0.2 m s^{-1} with a standard deviation of 1.9 m s^{-1}, and the periodic function fitted to the HMI flows has an amplitude of 2.3 ± 0.3 m s^{-1} on average. The corresponding meridional flows from GONG data (not shown) vary with a period that is roughly one year but changes with time, which might reflect the added complexity of merging images from different GONG sites. Fitting a function with a period of one year to the average over all latitudes, the phase is the same as that of the corresponding fit of HMI data. For GONG data, we calculated the average values over all latitudes for each rotation and subtracted the offset as a correction for this artifact. The mean offset is -0.6 m s^{-1} with a standard deviation of 1.9 m s^{-1}. The flow amplitudes are somewhat reduced at latitudes equatorward of 50° at this depth after applying the corrections. The overall flow pattern remains the same.

4. Summary and Discussion

We studied the systematic variations present in the zonal and meridional flows determined from GONG and SDO/HMI Dopplergrams using ring-diagram analysis. We measured the east–west and north–south variations in each flow component, as well as their variation with the B_0 angle. These systematics have been reported in previous studies (*e.g.* Komm, Howe, and Hill, 2009; Zhao *et al.*, 2012). Baldner and Schou (2012) have suggested that a radial velocity component might be introduced as a bias that is due to the varying height of the spectral-line formation from disk center to the solar limb in the solar atmosphere, which would explain the observed east–west trend in the zonal flow and would lead to a north–south trend in the meridional flow. Since the meridional flow is on average positive in the northern and negative in the southern hemisphere, a potential north–south trend cannot be easily determined. Its existence is thus a conjecture that seems to be justified by the results of Zhao *et al.* (2012), where the meridional flow derived from HMI intensity data and HMI Dopplergrams are in better agreement after the correction.

We find that the variation with depth of the average east–west trend of the zonal flow agrees in size and direction with the depth variation of the average north–south trend of the meridional flow derived from GONG and HMI data. This similarity indicates that the underlying cause might be the same in both cases. We described this systematic as a radial velocity function that varies with the distance from disk center, as suggested by Baldner and Schou (2012). We used a sum of radial polynomials (of Zernike polynomials) with zero

value and continuous derivative at disk center to describe this function and determined the fitting parameters with a linear regression. The resulting radial velocity component shows a maximum amplitude near 22.5° and 30° for flows derived from GONG and HMI data (Figure 6) and the fitting parameters are constant with time (Figure 8). The east–west trend of the zonal flow disappears after applying the correction for the radial velocity component and the north–south trend of the meridional flow is rather constant with depth. The fitting parameters are more or less constant with time and show little annual variation. These results support the assumption that these two trends are due to a radial velocity component of solar origin. The radial velocity component derived from GONG data differs from that derived from HMI data, which might reflect a change in the dynamics of the solar photosphere with height since GONG and HMI use different spectral lines and different velocity determination methods. The GONG data cover more than one solar cycle and the fitting parameters do not change systematically. If the radial velocity component is due to solar granulation (Baldner and Schou, 2012), then the relevant characteristics of the granulation are constant as well.

With this encouraging result, we attempted to describe the east–west variation of the meridional flow together with the north–south variation of the zonal flow as a rotational velocity component, which might be linked to an error in P angle. However, it is not that simple. Despite their similar variation with depth, the two trends have to be fitted independently because the north–south trend of the zonal flow is much larger in size than the east–west trend of the meridional flow and the east–west trend changes direction with the sign change of the B_0 angle. The meridional component consists mainly of an annual variation, while the zonal component consists of a non-zero contribution in addition to an annual variation. Since there is no obvious variation with the solar-cycle in the fitting parameters derived from the GONG data, the north–south variation of the zonal flow does not appear to be associated with magnetic activity either. These results indicate a geometric projection artifact. It is known that the ring-diagram power spectra suffer from the effect of projection (Jain *et al.*, 2013). The combined effect of projection and varying B_0 angle results in a variation in the geometric foreshortening. But the zonal and the meridional flow are affected in different ways. This might imply that the geometric projection artifact introduces a rotational velocity component that changes direction with the sign change of the B_0 angle and, in addition, introduces a "shear" component that affects mainly the zonal flows, leading to faster zonal flows in the southern and slower ones in the northern hemisphere. Another explanation is that the geometric artifact is not entirely radial but consists of a radial term and some nonradial distortion. For example, an "astigmatism" term could break the symmetry between the north–south trend of the zonal and the east–west trend of the meridional flow. We will explore the possibility of a nonradial term in the future.

A P-angle error is most likely the cause of the annual variation in the amplitude of the meridional flow that is 90° out of phase with the B_0 angle. The determination of the solar rotation axis by Beck and Giles (2005) and their comparison with previous results (Figure 5 in Beck and Giles, 2005) show that many results favor a value of $i \approx 7.15°$, which differs from the "classical" Carrington results of $i \approx 7.25°$ used. A pointing error of 0.1° would account for a 6 m s^{-1} flow (Beck and Giles, 2005). The amplitude of the annual variation is about 2 m s^{-1} and its mean is about 0.2 m s^{-1} for HMI data and -0.6 m s^{-1} for GONG data, which is small by comparison. A pointing error comparable to the accuracy of the instruments is thus sufficient to cause this annual variation. We can greatly reduce this artifact by fitting the variation with an appropriate periodic function and subtracting the fitted values.

The meridional and zonal flows derived from GONG and HMI agree better after applying the corrections, and the counter-cells that appear episodically at high latitudes are absent

from the corrected meridional flow. These results indicate that the east–west and north–south trends of the zonal and meridional velocities can be adequately represented by three velocity functions that vary with distance from disk center.

These systematics and their correction are crucial for a quantitative comparison of subsurface velocities derived from different instruments. Their correction will enable us to combine velocity data from GONG, HMI, and MDI measurements and to address questions, such as whether the amplitude of the meridional flow changes during a solar cycle and from cycle to cycle. The answers to these questions are vital for the understanding of the solar dynamo (*e.g.* Dikpati and Gilman, 2012; Karak and Choudhuri, 2012). However, the systematics will have only a small influence on synoptic flow maps because these flow values are heavily weighted toward the central meridian, which will drastically reduce the contribution of any east–west trend. We also subtracted a fit of the average in latitude of the zonal and meridional flow from each synoptic map, which removes much of any north–south trend especially at low- to mid-latitudes where active regions are located. As a consequence, maps of the solar-cycle variation of subsurface flows are also little affected since they are constructed from synoptic maps (*e.g.* Komm *et al.*, 2014). At high latitudes, the correction is required to remove episodic counter-cells from the meridional flow. On time scales of days, the systematics will have a substantial influence on subsurface flows, as noted in previous studies (*e.g.* Komm, Howe, and Hill, 2011).

References

Baldner, C.S., Schou, J.: 2012, Effects of asymmetric flows in solar convection on oscillation modes. *Astrophys. J. Lett.* **760**, L1. DOI. ADS.

Beck, J.G., Giles, P.: 2005, Helioseismic determination of the solar rotation axis. *Astrophys. J. Lett.* **621**, L153. DOI. ADS.

Bogart, R.S., Baldner, C., Basu, S., Haber, D.A., Rabello-Soares, M.C.: 2011a, HMI ring diagram analysis I. The processing pipeline. *J. Phys. Conf. Ser.* **271**, 012008. DOI. ADS.

Bogart, R.S., Baldner, C., Basu, S., Haber, D.A., Rabello-Soares, M.C.: 2011b, HMI ring diagram analysis II. Data products. *J. Phys. Conf. Ser.* **271**, 012009. DOI. ADS.

Corbard, T., Toner, C., Hill, F., Hanna, K.D., Haber, D.A., Hindman, B.W., Bogart, R.S.: 2003, Ring-diagram analysis with GONG++. In: Sawaya-Lacoste, H. (ed.) *GONG+ 2002. Local and Global Helioseismology: The Present and Future*, ESA Special Publication **517**, 255. ADS.

Dikpati, M., Gilman, P.A.: 2012, Theory of solar meridional circulation at high latitudes. *Astrophys. J.* **746**, 65. DOI. ADS.

Gizon, L., Birch, A.C.: 2005, Local helioseismology. *Living Rev. Solar Phys.* **2**, 6. DOI. ADS. http://solarphysics.livingreviews.org/Articles/lrsp-2005-6/.

Gizon, L., Birch, A.C., Spruit, H.C.: 2010, Local helioseismology: Three-dimensional imaging of the solar interior. *Annu. Rev. Astron. Astrophys.* **48**, 289. DOI. ADS.

González Hernández, I., Kholikov, S., Hill, F., Howe, R., Komm, R.: 2008, Subsurface meridional circulation in the active belts. *Solar Phys.* **252**, 235. DOI. ADS.

Greer, B., Hindman, B., Toomre, J.: 2013, Center-to-limb velocity systematic in ring-diagram analysis. In: Jain, K., Tripathy, S.C., Hill, F., Leibacher, J.W., Pevtsov, A.A. (eds.) *Fifty Years of Seismology of the Sun and Stars*, *ASP Conf. Ser.* **478**, 199. ADS.

Haber, D.A., Hindman, B.W., Toomre, J., Bogart, R.S., Larsen, R.M., Hill, F.: 2002, Evolving submerged meridional circulation cells within the upper convection zone revealed by ring-diagram analysis. *Astrophys. J.* **570**, 855. DOI. ADS.

Harvey, J.W., Hill, F., Hubbard, R.P., Kennedy, J.R., Leibacher, J.W., Pintar, J.A., Gilman, P.A., Noyes, R.W., Title, A.M., Toomre, J., Ulrich, R.K., Bhatnagar, A., Kennewell, J.A., Marquette, W., Patron, J., Saa, O., Yasukawa, E.: 1996, The Global Oscillation Network Group (GONG) project. *Science* **272**, 1284. DOI. ADS.

Harvey, J., Gillespie, B., Miedaner, P., Slaughter, C.: 1980, Synoptic solar magnetic field maps for the interval including Carrington rotation 1601 – 1680, May 5, 1973 – April 26, 1979. *NASA STI/Recon Technical Report N* **81**, 21003. ADS.

Jain, K., Tripathy, S.C., Basu, S., Baldner, C.S., Bogart, R.S., Hill, F., Howe, R.: 2013, Assessing ring-diagram fitting methods. In: Jain, K., Tripathy, S.C., Hill, F., Leibacher, J.W., Pevtsov, A.A. (eds.) *Fifty Years of Seismology of the Sun and Stars*, *ASP Conf. Ser.* **478**, 193. ADS.

Karak, B.B., Choudhuri, A.R.: 2012, Quenching of meridional circulation in flux transport dynamo models. *Solar Phys.* **278**, 137. DOI. ADS.

Komm, R., Howe, R., Hill, F.: 2009, Emerging and decaying magnetic flux and subsurface flows. *Solar Phys.* **258**, 13. DOI. ADS.

Komm, R., Howe, R., Hill, F.: 2011, Subsurface velocity of emerging and decaying active regions. *Solar Phys.* **268**, 407. DOI. ADS.

Komm, R., González Hernández, I., Hill, F., Bogart, R., Rabello-Soares, M.C., Haber, D.: 2013, Subsurface meridional flow from HMI using the ring-diagram pipeline. *Solar Phys.* **287**, 85. DOI. ADS.

Komm, R., Howe, R., González Hernández, I., Hill, F.: 2014, Solar-cycle variation of subsurface zonal flow. *Solar Phys.* **289**, 3435. DOI. ADS.

Scherrer, P.H., Bogart, R.S., Bush, R.I., Hoeksema, J.T., Kosovichev, A.G., Schou, J., Rosenberg, W., Springer, L., Tarbell, T.D., Title, A., Wolfson, C.J., Zayer, I., MDI Engineering Team: 1995, The solar oscillations investigation – Michelson Doppler imager. *Solar Phys.* **162**, 129. DOI. ADS.

Scherrer, P.H., Schou, J., Bush, R.I., Kosovichev, A.G., Bogart, R.S., Hoeksema, J.T., Liu, Y., Duvall, T.L., Zhao, J., Title, A.M., Schrijver, C.J., Tarbell, T.D., Tomczyk, S.: 2012, The Helioseismic and Magnetic Imager (HMI) investigation for the Solar Dynamics Observatory (SDO). *Solar Phys.* **275**, 207. DOI. ADS.

Schou, J., Scherrer, P.H., Bush, R.I., Wachter, R., Couvidat, S., Rabello-Soares, M.C., Bogart, R.S., Hoeksema, J.T., Liu, Y., Duvall, T.L., Akin, D.J., Allard, B.A., Miles, J.W., Rairden, R., Shine, R.A., Tarbell, T.D., Title, A.M., Wolfson, C.J., Elmore, D.F., Norton, A.A., Tomczyk, S.: 2012, Design and ground calibration of the Helioseismic and Magnetic Imager (HMI) instrument on the Solar Dynamics Observatory (SDO). *Solar Phys.* **275**, 229. DOI. ADS.

Snodgrass, H.B.: 1984, Separation of large-scale photospheric Doppler patterns. *Solar Phys.* **94**, 13. DOI. ADS.

Zaatri, A., Komm, R., González Hernández, I., Howe, R., Corbard, T.: 2006, North–south asymmetry of zonal and meridional flows determined from ring diagram analysis of GONG++ Data. *Solar Phys.* **236**, 227. DOI. ADS.

Zhao, J., Nagashima, K., Bogart, R.S., Kosovichev, A.G., Duvall, T.L. Jr.: 2012, Systematic center-to-limb variation in measured helioseismic travel times and its effect on inferences of solar interior meridional flows. *Astrophys. J. Lett.* **749**, L5. DOI. ADS.